Classification: Biological Sciences: Plant Biology

Arabidopsis and *Chlamydomonas* phosphoribulokinase crystal structures complete the redox structural proteome of the Calvin-Benson cycle

Short title: **Insight into chloroplast PRK structure**

Libero Gurrieri[a], Alessandra Del Giudice[b], Nicola Demitri[c], Giuseppe Falini[d], Nicolae Viorel Pavel[b], Mirko Zaffagnini[a], Maurizio Polentarutti[c], Pierre Crozet[e], Christophe H. Marchand[e], Julien Henri[e], Paolo Trost[a], Stéphane D. Lemaire[e], Francesca Sparla[a,1], Simona Fermani[d,1]

[a]Department of Pharmacy and Biotechnology – FaBiT, University of Bologna, 40126 Bologna, Italy

[b]Department of Chemistry, University of Rome 'Sapienza', 00185 Rome, Italy

[c]Elettra - Sincrotone Trieste, 34149, Basovizza - Trieste, Italy

[d]Department of Chemistry 'G. Ciamician', University of Bologna, 40126 Bologna, Italy

[e]Institut de Biologie Physico-Chimique, UMR8226, CNRS, Sorbonne Université, 75005 Paris, France

[1]To whom correspondence should be addressed:

Simona Fermani:

Address: Department of Chemistry 'G. Ciamician,' University of Bologna, Via Selmi 2 - 40126 Bologna, Italy

Phone: +39 051 2099475

Email address: simona.fermani@unibo.it

Francesca Sparla:

Address: Department of Pharmacy and Biotechnology – FaBiT, University of Bologna, Via Irnerio 42 - 40126 Bologna, Italy

Phone: +39 051 2091281

Email address: francesca.sparla@unibo.it

Abstract

In land plants and algae, the Calvin-Benson (CB) cycle takes place in the chloroplast, a specialized organelle in which photosynthesis occurs. Thioredoxins (TRXs) are small ubiquitous proteins, known to harmonize the two stages of photosynthesis through a thiol-based mechanism. Among the 11 enzymes of the CB cycle, the TRX target phosphoribulokinase (PRK) has yet to be characterized at the atomic scale. To accomplish this goal, we determined the crystal structures of PRK from two model species: the green alga *Chlamydomonas reinhardtii* (*Cr*PRK) and the land plant *Arabidopsis thaliana* (*At*PRK). PRK is an elongated homodimer characterized by a large central β-sheet of 18 strands, extending between two catalytic sites positioned at its edges. The electrostatic surface potential of the catalytic cavity has both a positive region suitable for binding the phosphate groups of substrates and an exposed negative region to attract positively charged TRX-f. In the catalytic cavity, the regulatory cysteines are 13 Å apart and connected by a flexible region exclusive to photosynthetic eukaryotes—the clamp loop—which is believed to be essential for oxidation-induced structural rearrangements. Structural comparisons with prokaryotic and evolutionarily older PRKs revealed that both *At*PRK and *Cr*PRK have a strongly reduced dimer interface and increased number of random coiled regions, suggesting that a general loss in structural rigidity correlates with gains in TRX sensitivity during the molecular evolution of PRKs in eukaryotes.

Keywords: 3D structure; Calvin-Benson cycle; phosphoribulokinase; redox-regulation; structural flexibility; thioredoxin

Significance Statement

In chloroplasts, five enzymes of the Calvin-Benson (CB) cycle are regulated by thioredoxins (TRXs). These enzymes have all been structurally characterized with the notable exception of phosphoribulokinase (PRK). Here, we determined the crystal structure of chloroplast PRK from two model photosynthetic organisms. Regulatory cysteines appear distant from each other and are

linked by a long loop that is present only in plant-type PRKs and allows disulfide bond formation and subsequent conformational rearrangements. Structural comparisons with ancient PRKs indicate that the presence of flexible regions close to regulatory cysteines is a unique feature that is shared by TRX-dependent CB cycle enzymes, suggesting that the evolution of the PRK structure has resulted in a global increase in protein flexibility for photosynthetic eukaryotes.

INTRODUCTION

Photosynthetic CO_2 fixation supports life on earth and is a fundamental source of food, fuel, and chemicals for human society. In the vast majority of photosynthetic organisms, carbon fixation occurs via the Calvin-Benson (CB) cycle (Fig. S1), a pathway that has been extensively studied at the physiological, biochemical, and structural levels. The CB cycle consists of 13 distinct reactions catalyzed by 11 enzymes (1) that are differentially regulated to coordinate the two stages of photosynthesis—electron transport and carbon fixation—and to couple them with the continuous changes in environmental light.

Thioredoxins (TRXs) are small thiol oxidoreductase enzymes that are widely distributed among the kingdoms of life. They reduce disulfide bonds in target proteins, controlling the redox state and modulating the activity of target enzymes (2). Compared to animals that usually possess 2–3 different TRXs, the plant thioredoxin system is much more complex. Looking only at the chloroplast, five different classes of TRXs are known (i.e., TRX-f, -m, -x, -y, and -z) with several isoforms composing many of these classes (2). Despite this diversity, TRXs are ancient and strongly evolutionarily conserved, consisting of a central core of a five-stranded β-sheet surrounded by four α-helices and an active site that protrudes from the protein's surface (3).

In TRX-dependent regulation, a small fraction of photosynthetic-reducing equivalents are transferred from photosystem I to several chloroplast TRXs, which in turn reduce key enzymes of the CB cycle, regulating their activity (1). Among the five classes of chloroplast TRXs, class f displays a high specificity towards CB cycle enzymes. In both plants and algae, the activities of

83 fructose-1,6-bisphosphatase (FBPase) (4, 5), sedoheptulose-1,7-bisphosphatase (SBPase) (5), PRK
84 (6), and the AB isoform of NADP-glyceraldehyde 3-phosphate dehydrogenase (AB-GAPDH) (7) in
85 plants and of phosphoglycerate kinase (PGK) (8) in *Chlamydomonas* are directly linked to light by
86 a thiol-based mechanism driven by TRX (Fig. S1). In addition, PRK forms a regulatory complex
87 with the redox-sensitive CP12 and the homotetrameric NADP-GAPDH (A_4-GAPDH) (9-11). The
88 formation of this ternary complex occurs in both plants and algae, and causes an almost complete
89 inhibition of PRK activity (12).
90 In contrast to the canonical WCGPC active site of TRXs, no thioredoxin-recognition signature is
91 found in these enzymes. A structural comparison of SBPase and FBPase highlights how evolution
92 has adopted different strategies for modeling protein structure to achieve the same TRX-dependent
93 redox control (5). Of the three enzymes regulated by TRX whose 3D structures are available, a pair
94 of redox-sensitive cysteines was found to be located in completely different regions. In AB-
95 GAPDH, these cysteines are located in a C-terminal extension (CTE) (7); in SBPase, they are
96 present at the dimer interface (5); and in FBPase, they are solvent exposed and distant from the
97 sugar-binding site (4, 5).
98 To complete the structural redox proteome of the CB cycle enzymes and identify the common
99 feature behind the acquisition of TRX-mediated redox control, the crystal structures of PRK from
100 two model species—the green alga *Chlamydomonas reinhardtii* and the land plant *Arabidopsis*
101 *thaliana*—were determined and compared to those of other TRX-controlled enzymes. Our results
102 strongly show that the acquisition of a TRX-targeted motif positively correlates with the acquisition
103 of flexibility in the target proteins, consistent with the observation that the entropic contribution
104 obtained from the reduction of the oxidized target enzyme is the main driving force of the redox
105 control mediated by TRXs (13).
106

107 **RESULTS AND DISCUSSION**

108 **Three-dimensional structures of *Cr*PRK and *At*PRK in solution and in crystal form**

109 To gain insight into the molecular mechanism of regeneration of the five-carbon sugar ribulose-1,5-
110 bisphosphate (Fig. S1) and of its redox control by dithiol/disulfide exchange, the crystal structures
111 of *Cr*PRK and *At*PRK were determined at 2.6 Å and 2.5 Å, respectively, and compared with those
112 obtained in solution by size-exclusion chromatography-small angle X-ray scattering (SEC-SAXS).
113 Both enzymes are dimers of two identical monomers connected by a 2-fold noncrystallographic axis
114 (Fig. 1). They are structurally similar, and their superimposition results in a root main square
115 deviation of 0.61 Å (on 330 aligned residues) for *Cr*PRK and 1.03 Å (on 328 aligned residues) for
116 *At*PRK.
117 Each monomer contains a central nine-stranded mixed β-sheet (β1−β9) surrounded by eight α-
118 helices (α1, α3–α9), four additional β-strands (β1'–β4'), and one additional α-helix (α2; Figs. 2 and
119 S2).
120 The *At*PRK crystal structure confirms the elongated shape of the oxidized protein previously
121 observed by SAXS analysis (10) but appears less bent and twisted. Structural information regarding
122 *Cr*PRK in solution provides a single recognizable species with an R_g value of 35 ± 1 Å and an
123 estimated molecular weight around 70 kDa (Fig. S3 and Table S1). The SAXS scattering profile can
124 be completely superimposed on the theoretical profile calculated from the *Cr*PRK crystal structure
125 (Fig. 3*A*), indicating that the solved crystal structure closely matches the structure of the protein in
126 solution (Fig. 3*B*).
127 The active sites (one per monomer) are located in an elongated cavity at the edges of the dimer
128 (Figs. 4*A* and S4*A*). In the *Cr*PRK structure, the active site cavity is marked by a sulfate ion derived
129 from the crystallization medium that highlights the position occupied by the phosphate group of the
130 substrate ribulose 5-phosphate (Ru5P) (Fig. 4*A* and *B*). The anion is stabilized by the side chains of
131 Arg64, Arg67, and Tyr103, and by the main chain carbonyl group of His105 (Fig. S5). Except for
132 Arg67, these residues are strictly conserved in PRKs (Fig. S6*A*). The catalytic role of the invariant
133 Arg64 was also confirmed in *C. reinhardtii* (14). In addition, Arg64 was found to play a major role
134 in the interaction of PRK with A_4-GAPDH during the formation of the regulatory ternary complex

135 (14). Consistent with this finding, Arg64 faces out at the far end of the dimer (Fig. 1 and Table S2).
136 The active site also contains a pair of regulatory cysteines (Figs. 4*A* and *B* and S4*A* and *B*); Cys15
137 in *At*PRK and Cys16 in *Cr*PRK are located within the P-loop (Walker A) (15) and belong to the
138 ATP-binding site (16). Additionally, Cys54 in *At*PRK and Cys55 in *Cr*PRK are located at the C-
139 terminal end of strand β2 and compose the intermolecular mixed disulfide with TRX-f (6) (Figs. 2
140 and S2).

141 **Redox properties of *Cr*PRK and *At*PRK**

142 Despite the role that PRK plays in photosynthesis, putative PRK sequences have also been found in
143 heterotrophic prokaryotes. Phylogenetic analyses performed on 69 PRK sequences, including 31
144 from nonphotosynthetic prokaryotes, clearly show a first evolutionary separation between Bacteria
145 and Archaea. Cyanobacterial and eukaryotic PRKs emerged as the third clade from Archaea (Fig.
146 S6*B*). Single PRK structures from the anoxygenic photosynthetic bacterium *Rhodobacter*
147 *sphaeroides* (*Rs*PRK; PDB ID code 1A7J) (17) and the nonphotosynthetic Archaea
148 *Methanospirillum hungatei* (*Mh*PRK; PDB ID code 5B3F; 18) have been reported. Both *Rs*PRK
149 and *Mh*PRK sequences are shorter than plant PRKs with a low sequence identity (Fig. S7). All
150 PRKs from bacteria (type I PRKs; 19), including phototrophic organisms, are octamers (~32-kDa
151 subunits) that are allosterically activated by NADH and inhibited by AMP (20). Archaea,
152 cyanobacteria, and eukaryotic (i.e., plant-type) PRKs are dimers (~40-kDa subunits; type II PRKs)
153 (19) with no allosteric regulation (11, 21). While little is known about the regulation of archaeal
154 PRKs, in oxygenic phototrophs from ancient cyanobacteria to modern flowering plants, it is well
155 established that PRK forms a complex with A_4-GAPDH and the regulatory protein CP12 at low
156 NADP(H)/NAD(H) ratios (22, 23). Moreover, cyanobacterial PRKs are inhibited by AMP via the
157 cyanobacteria-specific fusion protein CBS-CP12 (24), whereas plant-type PRKs are directly
158 regulated by the TRX-dependent interconversion of specific dithiol-disulfide bridges (6). To date,
159 no experimental evidence of the direct regulation of cyanobacterial PRKs by TRXs has been
160 reported.

161 Regulatory cysteines Cys15/16 and Cys54/55 in *At*PRK and *Cr*PRK, respectively, protrude from
162 the catalytic cavity (Figs. 4*A* and S4*A*) and are thus available to interact with TRX (Table S2). In
163 addition, both PRKs share similar redox properties with comparable midpoint redox potentials (–
164 312 ± 3 mV for *Cr*PRK and –330 mV for *At*PRK) (23) and pK_a values (6.79 ± 0.01 for *Cr*PRK and
165 6.95 ± 0.13 for *At*PRK) (Figs. 4*C* and S4*C*). These slightly acidic values are supported by the
166 molecular environment around Cys15/16, as the thiol groups form hydrogen bonds with the main
167 chain atoms of two nearby residues (i.e., Asp13 and Ser14 in *Cr*PRK and Asp12 and Ser13 in
168 *At*PRK) and with the amino and carboxyl groups of Lys156 and Asp13 in *Cr*PRK or Lys151 in
169 *At*PRK (Figs. 4*D* and S4*D*). All of these residues are strictly conserved in type I PRKs (Fig. S6*A*).
170 Furthermore, the proximity of Cys15/16 to the positive N-terminal end of helix α1 contributes to a
171 low pK_a value (Figs. 4*D* and S4*D*).
172 The pH and temperature dependence of *At*PRK and *Cr*PRK are also comparable, although the algal
173 enzyme has a wider range of activity at higher temperatures and lower pH values (Fig. S8). The pair
174 of cysteines involved in TRX regulation is also present in the TRX-insensitive PRK in
175 cyanobacteria (Fig. S6*A*). However, cyanobacterial PRKs lack an unstructured amino acid stretch
176 (25)—here named clamp loop—which connects the regulatory cysteines whose thiol groups are
177 separated by more than 13 Å, as found in plant-type PRKs (Figs. 4*A* and S4*A*). The clamp loop
178 connects α1 and β2 (Figs. 1 and S7) and possibly confers the flexibility necessary to permit the
179 conformational changes required for disulfide formation. This bond would thus allow the narrowing
180 of the catalytic cavity and the inhibition of enzymatic activity (Fig. 5*A*). Similarly, a comparison of
181 the chloroplast and redox-sensitive isoforms of FBPase (5) and AB-GAPDH (7) with their cytosolic
182 and redox-insensitive counterparts reveals that the acquisition of TRX-mediated regulation is
183 accompanied by the appearance of loops presumably required for the approach of the two cysteines
184 involved in the formation of the regulatory disulfide bond.
185 The electrostatic surface potential of the catalytic cavity reveals an elongated positive region on the
186 bottom and a negative region on the side (Figs. 4*B* and S4*B*), the former suitable for binding the

187 phosphate groups of substrates (i.e., ATP and Ru5P) and the latter relevant for the recognition and
188 positioning of TRX, as proposed for FBPase (13, 26). Compared to TRX-m, TRX-f2 is more
189 efficient in the reductive activation of both *At*PRK (27) and *Cr*PRK (Fig. 5*B*). Accordingly, the
190 structural model of *At*TRX-f1 and the crystal structure of *Cr*TRX-f2 (28) show that the catalytic
191 cysteines are surrounded by a large positive region, less extended in TRX-m (Fig. S9). This finding
192 suggests that the early stages of pairing between TRX and PRK are mainly governed by
193 electrostatic interactions between exposed regions of the two proteins (26).
194 Moreover, it has been reported that the oxidized state of target proteins is an essential feature for
195 TRX target recognition, since disulfide formation does not confer any specific conformational
196 change in TRXs structure (13). Indeed, the disulfide bond between the two distant regulatory
197 cysteines introduces a significant conformational constraint that decreases the overall entropy of
198 PRK. Therefore, a favorable entropic contribution is proposed to be the main driving force of the
199 reduction of PRK by TRXs.
200 **Dimer interface and flexible regions**
201 Dimer interfaces consist of large contact areas in octameric *Rs*PRK (1,667 $Å^2$) (17) and dimeric
202 *Mh*PRK (1,695 $Å^2$; Fig. S10) (18), and a small area in eukaryotic PRK. The dimer interfaces in
203 *Cr*PRK (545.6 $Å^2$) and *At*PRK (560.3 $Å^2$) are exclusively formed by β7, which is located in an
204 antiparallel position to its partner (Figs. 1, 2, and S2), suggesting a less rigid structure. Since
205 cyanobacterial and eukaryotic PRKs are found together with CP12, the greater flexibility of PRK
206 could enable the formation of regulatory GAPDH/CP12/PRK complexes (9-11). Moreover, *At*PRK
207 and *Cr*PRK are characterized by an increased number of exposed random coiled regions (Fig. 1 and
208 Table S3), some of which show a poor or absent electron density, indicative of highly flexible and
209 disordered regions (Fig. S11). Two such regions are common to algal and plant enzymes, whereas
210 the presence of a third region is exclusive to *At*PRK.
211 The long loop between helices α5 and α6 (Fig. S11) contains the highly conserved catalytic Asp160
212 or Arg159 and Arg164 residues involved in Ru5P binding (29, 30). A second flexible region,

213 corresponding to the loop between β7 and β8, contains Cys243 and Cys249 (Figs. 1 and S11). In
214 both PRK structures, this portion is so flexible that the two thiol groups are far from each other in
215 one monomer and closer to one another in the other; however, in contrast to *At*PRK, they are not
216 oxidized in *Cr*PRK (Figs. 1 and S12). This result is in agreement with the observation that in
217 *Cr*PRK, the disulfide bond between Cys243 and Cys249 only forms via an interaction with CP12
218 (31). This interaction is an essential step for the assembly of PRK and A_4-GAPDH, leading to the
219 regulatory complex GAPDH/CP12/PRK (32, 33).
220

221 **CONCLUDING REMARKS**

222 TRXs are widespread regulatory proteins whose structure is strongly conserved throughout
223 evolution. Fascinating experiments in paleobiochemistry conducted on seven "resurrected" TRXs
224 dating back to the Precambrian era showed that only small differences in the length of helix α1 were
225 found to occur over 4 Gyr of evolution (3). How evolution affected the TRX dependence of
226 enzymes in the CB cycle is still a mystery. After studying the five CB cycle enzymes whose 3D
227 structures have been solved or modeled (Fig S1), several strategies were adopted to establish their
228 dependency on the same regulator. In fact, each of these five proteins are regulated by TRX in a
229 different way. In FBPase and SBPase, the TRX-binding site is far from the conserved sugar-binding
230 domain (5). In FBPase, upon reduction, the substrate-binding site adopts a catalytically competent
231 conformation due to the loosening of secondary structures (4, 5). In AB-GAPDH, the redox-active
232 cysteines are found in the highly flexibly CTE, which is characteristic of B-subunits, and when
233 oxidized, the last residue in the CTE blocks the NAPDH-binding site (7). Similarly, a change in
234 protein flexibility is believed to enable the regulation of *Chlamydomonas* PGK in which the
235 formation of the regulatory disulfide appears to lower catalytic efficiency by decreasing the
236 flexibility required to approach the substrates (8). Finally, we report that the regulatory pair of
237 cysteines in PRK is embedded in the substrate-binding site and that oxidation can be achieved by
238 the presence of the flexible clamp loop.

239 We conclude that a common strategy has allowed the acquisition of TRX dependence of the CB
240 cycle enzymes during evolution—the introduction of flexible regions. This strategy is in sharp
241 contrast to the evolutionary rigidity of the TRX structure.
242

243 **MATERIALS AND METHODS**

244 **Protein Expression and Purification**

245 Recombinant *At*PRK and *Cr*PRK were expressed in *E. coli* BL21(DE3) strain (New England
246 Biolabs) harboring the pET-28 expression vector (Novagen) containing the coding sequence of the
247 mature form of both enzymes (Fig. S7). *At*PRK was expressed and purified as previously described
248 (33). The sequence coding for *Cr*PRK was cloned in frame with a 6xHis-Tag and a thrombin
249 cleavage site at the 5' end of the nucleotide sequence. *Cr*PRK was purified by Chelating Sepharose
250 Fast Flow (GE Healthcare) column, following the manufacturer instruction. Immediately after
251 elution, *Cr*PRK was desalted in 30 mM Tris-HCl, 1 mM EDTA, pH 7.9 by PD-10 Desalting
252 Columns (GE Healthcare). The 6xHis-Tag was removed by overnight digestion with thrombin
253 protease. Samples purity was checked by 12.5% SDS-PAGE and purified proteins were quantified
254 by absorbance at 280 nm (Nanodrop; Thermo Scientific) using the following extinction coefficients:
255 ε*At*PRK 31985 M^{-1} cm^{-1}; ε*Cr*PRK 35995 M^{-1} cm^{-1} and molecular weights: *At*PRK 38784.23 g mol^{-1}
256 and *Cr*PRK 40790.7 g mol^{-1}. Proteins were stored at -80 °C.
257 When required, oxidized and reduced *At*PRK and *Cr*PRK were prepared by incubation at 25°C for
258 2-3 h in the presence of 40 mM trans-4,5-dihydroxy-1,2-dithiane (oxidized DTT) or 1,4-
259 dithiothreitol (reduced DTT). Following incubation, samples were desalted in 30 mM Tris-HCl, 1
260 mM EDTA, pH 7.9 through NAP-5 column (GE Healthcare) and brought to the desired
261 concentration either by dilution or by concentration through Amicon-Ultra device (Millipore; cut-
262 off 10 kDa).

263 **Activity Assay and Determination of pH and Temperature Dependence**

264 Phosphoribulokinase activity was measured spectrophotometrically (Cary 60 UV-Vis; Agilent) as
265 previously described (34). The pH dependence of purified enzymes was determined in Britton-
266 Robinson buffer for pH values ranging from 4.0 to 8.5. For pH ranging from 9 to 10, 100 mM
267 Glycine buffer was used. Activities were measured on two independent protein batches and are
268 expressed as percentage of the highest measured activity. Temperature dependence was evaluated
269 on aliquots of *At*PRK and *Cr*PRK incubated for 20 min at temperatures ranging from 20°C to 60°C.
270 Following incubation, the activity was assayed at 25°C. Activities were measured on two
271 independent protein purifications and are expressed as percentage of the highest measured activity.

272 **Thioredoxin Specificity, Redox Titration**

273 Thioredoxin specificity for activation of oxidized *Cr*PRK (2 µM) was measured in the presence of
274 0.2 mM reduced DTT and *C. reinhardtii* recombinant TRX-f2 and TRX-m (5 µM each), as
275 previously described (27). At different incubation times, PRK activity was measured. To determine
276 the midpoint redox potential of *Cr*PRK, three independent redox titrations were performed. Briefly,
277 a mixture containing pure recombinant *Cr*PRK (12 µM), commercial *E. coli* thioredoxin (1 mg ml^{-}
278 ^{1}) and 20 mM DTT, at different reduced to oxidized ratios, were incubated for 3 h at 25°C before
279 measuring PRK activity. The obtained curves were fitted by non-linear regression (CoStat, Co-Hort
280 Software) to the Nernst equation.

281 **Determination of the pK_a Values of the Catalytic Cysteines**

282 The determination of pK_a values for both *Cr*PRK and *At*PRK was performed as previously
283 described (35). Briefly, PRK activity was measured on reduced PRK samples (2 µM) following 20
284 min of incubation at 25°C in the presence or absence of 0.2 mM iodoacetamide (IAM). Incubations
285 were performed in different buffers within a 4.5-10 pH range. Aliquots of 10-20 µl were used to
286 measure PRK activity in 1 ml of assay mixture. The residual activity was expressed as percentage
287 of inhibition between IAM-treated and untreated samples, and expressed as a function of pH. The
288 obtained curves were fitted by non-linear regression (CoStat, Co-Hort Software) to modified
289 Henderson-Hasselbalch equation.

290 **Crystallization Data Collection and Structure Refinement.**

291 Reduced *Cr*PRK was concentrated at 10 mg ml^{-1} in 30 mM Tris-HCl, 1 mM EDTA, pH 7.9.
292 Reduced *At*PRK was concentrated at 10 mg ml^{-1} in 25 mM potassium phosphate buffer solution,
293 pH 7.5. They were crystallized by the vapor diffusion method at 293 K with sitting drop in 22% w/v
294 PEG MME 5K, 0.1 M MES, pH 6.5, 0.2 M ammonium sulfate for *Cr*PRK, and hanging drop in 1.5
295 M sodium malonate, pH 5.0, for *At*PRK. The crystals obtained were analyzed by X-ray diffraction,
296 and the structures were solved by molecular replacement. The refinement was performed with
297 REFMAC 5.8.0135 (36) selecting 5% of reflections for R_{free} (for details, see SI Appendix, SI
298 Materials and Methods).

299 **Small Angle X-ray Scattering Data Collection and Analysis**

300 Small angle X-ray scattering (SAXS) data were collected at the BioSAXS beamline BM29 (37) at
301 European Synchrotron Radiation Facility (ESRF, Grenoble) and the data collection parameters are
302 reported in Table S4. A size-exclusion chromatography SEC-SAXS experiment was performed
303 using a HPLC system (Shimadzu) directly connected to the measurement capillary. All the details
304 about experimental procedures and data analysis are listed in SI Appendix, SI Materials and
305 Methods.

306 **Modeling from SAXS Data**

307 The experimental SAXS profile of the *Cr*PRK dimer was fitted with the theoretical profile
308 calculated from the atomic coordinates using CRYSOL3 (38) with default parameters. In addition,
309 low-resolution models of the CrPRK dimer based on the SAXS profile were built using the ab initio
310 program GASBOR (39). All details are reported in SI Appendix, SI Materials and Methods.

311 **Data Availability**

312 Atomic coordinates and structure factors have been deposited in the Protein Data Bank (PDB) under
313 accession codes 6H7G and 6H7H for *Cr*PRK and *At*PRK, respectively. The SEC-SAXS data of
314 *Cr*PRK have been deposited in SASBDB with accession code SASDDH9.

315

ACKNOWLEDGEMENTS

We sincerely thank Prof. Bob B. Buchanan for offering comments and constructive suggestions on the content of the manuscript. We thank the Elettra and European Synchrotron Radiation Facility for allocation of X-ray diffraction and SAXS beam time (BAG proposal MX686 and MX1750) and the staff of beamlines XRD1 (Elettra) and BM29 (ESRF) for technical support. This work was supported by the Italian Minister of Education, Research and University (MIUR) grant FIRB2003 (P.T.); by University of Bologna grant FARB2012 (F.S., S.F., and M.Z.); by CNRS, Sorbonne Université, Agence Nationale de la Recherche Grant 17-CE05-0001; and CalvinDesign and LABEX DYNAMO ANR-LABX-011 (J.H., S.D.L., and P.C.). S.F. thanks the Consorzio Interuniversitario di Ricerca in Chimica dei Metalli nei Sistemi Biologici (CIRCMSB).

326 **REFERENCES**

327 1. Michelet L, et al. (2013) Redox regulation of the Calvin-Benson cycle: Something old,
328 something new. *Front Plant Sci* 4:470.
329 2. Geigenberger P, Thormählen I, Daloso DM, Fernie AR (2017) The Unprecedented Versatility
330 of the Plant Thioredoxin System. *Trends Plant Sci* 22(3):249-262.
331 3. Ingles-Prieto A, et al. (2013) Conservation of protein structure over four billion years. *Structure*
332 21(9):1690-1697.
333 4. Chiadmi M, Navaza A, Miginiac-Maslow M, Jacquot JP, Cherfils J (1999) Redox signalling in
334 the chloroplast: Structure of oxidized pea fructose-1,6-bisphosphate phosphatase. *EMBO J*
335 18(23):6809–6815.
336 5. Gütle DD, et al. (2016) Chloroplast FBPase and SBPase are thioredoxin-linked enzymes with
337 similar architecture but different evolutionary histories. *Proc Natl Acad Sci USA* 24(113):6779–
338 6784.
339 6. Brandes HK, Larimer FW, Hartman FC (1996) The molecular pathway for the regulation of
340 phosphoribulokinase by thioredoxin f. *J Biol Chem* 271(7):3333-3335.
341 7. Fermani S, et al. (2007) Molecular mechanism of thioredoxin regulation in photosynthetic
342 A2B2-glyceraldehyde-3-phosphate dehydrogenase. *Proc Natl Acad Sci USA* 26(104):11109–
343 11114.
344 8. Morisse S, et al. (2014). Thioredoxin-dependent redox regulation of chloroplastic
345 phosphoglycerate kinase from *Chlamydomonas reinhardtii*. *J Biol Chem* 289(43):30012-30024.
346 9. Mouche F, Gontero B, Callebaut I, Mornon J-P, Boisset N (2002). Striking conformational
347 change suspected within the phosphoribulokinase dimer induced by interaction with GAPDH. *J*
348 *Biol Chem* 277(8):6743–6749.
349 10. Del Giudice A, et al. (2015) Unravelling the shape and structural assembly of the photosynthetic
350 GAPDH-CP12-PRK complex from *Arabidopsis thaliana* by small-angle X-ray scattering
351 analysis. *Acta Crystallogr D Biol Crystallogr* 71(Pt 12):2372–2385.

11. Mcfarlane C, Shah N, Kabasakal BV, Cotton CAR, Bubeck D, Murray JW (2018) Structural basis of light-induced redox regulation in the Calvin cycle. *bioRxiv* 414334; doi: https://doi.org/10.1101/414334
12. Marri L, Thieulin-Pardo G, Lebrun R, Puppo R, Zaffagnini M, Trost P, Gontero B, Sparla F (2014) CP12-mediated protection of Calvin-Benson cycle enzymes from oxidative stress. *Biochimie* 97:228-237.
13. Palde PB, Carroll KS (2015) A universal entropy-driven mechanism for thioredoxin-target recognition. *Proc Natl Acad Sci USA* 112(26):7960–7965.
14. Avilan L, Gontero B, Lebreton S, Ricard J (1997) Information transfer in multienzyme complexes 2. The role of Arg64 of *Chlamydomonas reinhardtii* phosphoribulokinase in the information transfer between glyceraldehyde-3-phosphate dehydrogenase and phosphoribulokinase. *Eur J Biochem* 250(2):296–302.
15. Walker JE, Saraste M, Runswick MJ, Gay NJ (1982) Distantly related sequences in the alpha- and beta-subunits of ATP synthase, myosin, kinases and other ATP-requiring enzymes and a common nucleotide binding fold. *EMBO J.* 1(8):945–951.
16. Brandes HK, Hartman FC, Lu TY, Larimer FW (1996) Efficient expression of the gene for spinach phosphoribulokinase in *Pichia pastoris* and utilization of the recombinant enzyme to explore the role of regulatory cysteinyl residues by site-directed mutagenesis. *J Biol Chem* 271(11):6490-6496.
17. Harrison DH, Runquist JA, Holub A, Miziorko HM (1998) The crystal structure of phosphoribulokinase from *Rhodobacter sphaeroides* reveals a fold similar to that of adenylate kinase. *Biochemistry* 37(15):5074–5085.
18. Kono T, et al. (2017) A RuBisCO-mediated carbon metabolic pathway in methanogenic archaea. *Nat. Commun.* 8:14007.
19. Martin W, Schnarrenberger C (1997) The evolution of the Calvin cycle from prokaryotic to eukaryotic chromosomes: a case study of functional redundancy in ancient pathways through

378 endosymbiosis. *Curr Genet* 32(1):1-18.

379 20. Kung G, Runquist JA, Miziorko HM, Harrison DH (1999) Identification of the allosteric
380 regulatory site in bacterial phosphoribulokinase. *Biochemistry* 38(46):15157–15165.

381 21. Porter MA, Hartman FC (1990) Exploration of the function of a regulatory sulfhydryl of
382 phosphoribulokinase from spinach. *Arch Biochem Biophys* 281(2):330–334.

383 22. Tamoi M, Miyazaki T, Fukamizo T, Shigeoka S (2005) The Calvin cycle in cyanobacteria is
384 regulated by CP12 via the NAD(H)/NADP(H) ratio under light/dark conditions. *Plant J*
385 42(4):504–513.

386 23. Marri L, Trost P, Pupillo P, Sparla F (2005) Reconstitution and properties of the recombinant
387 glyceraldehyde-3-phosphate dehydrogenase/CP12/phosphoribulokinase supramolecular
388 complex of Arabidopsis. *Plant Physiol* 139(3):1433–1443.

389 24. Hackenberg C, et al. (2018) Structural and functional insights into the unique CBS-CP12 fusion
390 protein family in cyanobacteria. *Proc Natl Acad Sci U S A* 115(27):7141-7146.

391 25. Kobayashi D, Tamoi M, Iwaki T, Shigeoka S, Wadano A (2003) Molecular characterization and
392 redox regulation of phosphoribulokinase from the cyanobacterium Synechococcus sp. PCC
393 7942. *Plant Cell Physiol.* 44(3):269–276.

394 26. Mora-Garcia S, Rodríguez-Suárez R, Wolosiuk RA (1997) Role of electrostatic interactions on
395 the affinity of thioredoxin for target proteins. Recognition of chloroplast fructose-1,6-
396 bisphosphatase by mutant Escherichia coli thioredoxins. *J Biol Chem* 273(26):16273–16280.

397 27. Marri, L. *et al.* (2009) Prompt and easy activation by specific thioredoxins of Calvin cycle
398 enzymes of *Arabidopsis thaliana* associated in the GAPDH/CP12/PRK supramolecular
399 complex. *Mol. Plant.* 2(2):259–269.

400 28. Lemaire SD, et al. (2018) Crystal Structure of chloroplastic thioredoxin f2 from
401 *Chlamydomonas reinhardtii* reveals distinct surface properties. *Antioxidants* 7(12):171.

402 29. Charlier HA Jr, Runquist JA, Miziorko HM (1994) Evidence Supporting Catalytic Roles for
403 Aspartate Residues in Phosphoribulokinase. *Biochemistry* 33(31):9343–9350.

404 30. Runquist JA, Harrison DH, Miziorko HM (1999) *Rhodobacter sphaeroides*
405 phosphoribulokinase: identification of lysine-165 as a catalytic residue and evaluation of the
406 contributions of invariant basic amino acids to ribulose 5-phosphate binding. *Biochemistry*
407 38(42):13999–14005.
408 31. Thieulin-Pardo G, Remy T, Lignon S, Lebrun R, Gontero B (2015) Phosphoribulokinase from
409 *Chlamydomonas reinhardtii*: a Benson-Calvin cycle enzyme enslaved to its cysteine residues.
410 *Mol. Biosyst.* 11(4):1134–1145.
411 32. Graciet E, et al. (2003) The small protein CP12: a protein linker for supramolecular complex
412 assembly *Biochemistry* 42(27):8163–8170.
413 33. Marri L, et al. (2008) Spontaneous assembly of photosynthetic supramolecular complexes as
414 mediated by the intrinsically unstructured protein CP12. *J. Biol. Chem.* 283(4):1831-1838.
415 34. Roesler KR, Ogren WL (1990) *Chlamydomonas reinhardtii* phosphoribulokinase: sequence,
416 purification and kinetics. *Plant Physiol* 93(1):188-193.
417 35. Bedhomme M, et al. (2012) Glutathionylation of cytosolic glyceraldehyde-3-phosphate
418 dehydrogenase from the model plant *Arabidopsis thaliana* is reversed by both glutaredoxins and
419 thioredoxins in vitro. *Biochem J* 445(3):337–347.
420 36. Cowtan K (2006) The Buccaneer software for automated model building. 1. Tracing protein
421 chains. *Acta Crystallogr D Biol Crystallogr* 62(Pt 9):1002–1011.
422 37. Brennich ME, et al. (2016) Online data analysis at the ESRF bioSAXS beamline, BM29. *J Appl*
423 *Crystallogr* 49:203–212.
424 38. Rambo RP, Tainer JA (2013) Accurate assessment of mass, models and resolution by small-
425 angle scattering. Nature 496(7446):477–481.
426 39. Franke D, et al. (2017) ATSAS 2.8: A comprehensive data analysis suite for small-angle
427 scattering from macromolecular solutions. J Appl Crystallogr 50(Pt 4):1212–1225.

428 **FIGURE LEGENDS**

429 **Fig. 1.** The crystal structure of photosynthetic PRK. Representation of the overall crystal structure
430 of reduced phosphoribulokinase (PRK) from (*A*) *Chlamydomonas reinhardtii* and (*B*) *Arabidopsis*
431 *thaliana*. The P-loop is highlighted in green and light-blue, and the clamp loop in orange and
432 yellow, respectively. Each monomer contains two pairs of cysteines, one in the active site (Cys16
433 and Cys55 for *Cr*PRK and Cys15 and Cys54 for *At*PRK) and one in the dimer interface close to the
434 C-terminal end of the protein chain (Cys243 and Cys249). Cysteine residues are indicated and
435 represented as sticks. In *At*PRK, a pair of C-terminal cysteines forms a disulfide bond. *Cr*PRK
436 binds two sulfate ions (one for each monomer), represented as spheres, from the crystallization
437 solution. Arg64, represented as sticks, is one of the residues stabilizing the anions.

438

439 **Fig. 2.** The crystal structure of the *Cr*PRK monomer. (*A*) Topology diagram: The monomer is
440 composed of a mixed β-sheet of nine strands, nine α-helices, and four additional small β-strands
441 indicated by β'. (*B*) Representation of the structure of the monomer: The central β-sheet is
442 sandwiched between helices α3, α4, and α6 and helices α1, α7, α8, and α9. Strand β7 is located in
443 the dimer interface, whereas the four additional β-strands (β1' to β4') form the edge of the dimer.

444

445 **Fig. 3.** SAXS analysis of *Cr*PRK. (*A*) Superimposition of the experimental SAXS scattering profile
446 (black) and the theoretical SAXS curve (red), calculated from the *Cr*PRK crystal structure (upper
447 graph). The lower graph shows the residuals obtained by the difference between the experimental
448 and calculated intensities. (*B*) Comparison between the ab initio model (surface representation) and
449 the crystal structure (ribbon representation) of *Cr*PRK, showing an excellent agreement between the
450 two models.

451

452 **Fig. 4.** The active site and TRX-dependent regulation of *Cr*PRK. (*A*) The catalytic cavity is shown.
453 The distance between the regulatory cysteines is greater than 13 Å. (*B*) The electrostatic surface

454 potential of the catalytic cavity. The bottom of the catalytic cavity is marked by a positive potential.
455 The negative potential observed in the left side of the cavity is thought to be involved in the correct
456 positioning of TRX close to the regulatory cysteines. (*C*) The pK_a of Cys16 was determined by
457 measuring the IAM-mediated inactivation as a function of pH. (*D*) The molecular environment of
458 Cys16, considering a sphere of 5 Å centered on its thiol group. The hydrogen bonds between the
459 thiol group and the neighboring residues, and the corresponding distances are shown.

460

461 **Fig. 5.** The clamp loop and TRX-dependent regulation of *Cr*PRK. (*A*) A schematic representation
462 of the proposed role for the clamp loop and conformational changes occurring in the chloroplast
463 PRK upon TRX binding. (*B*) Activation kinetics by plastidial *C. reinhardtii* TRX-f2 and -m, and
464 DTT.

465 **Figure 1**

466

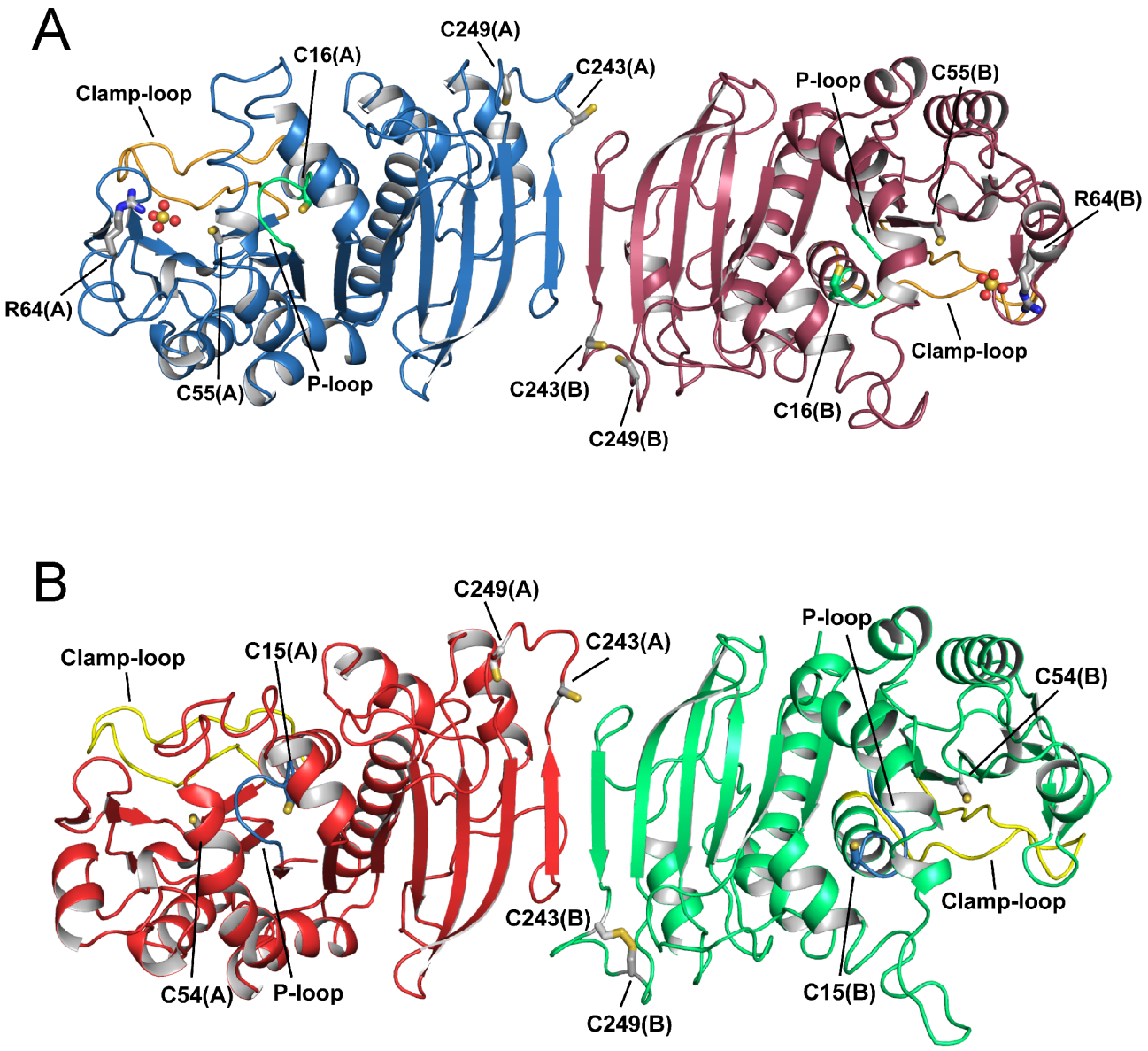

467
468

469 **Figure 2**

470

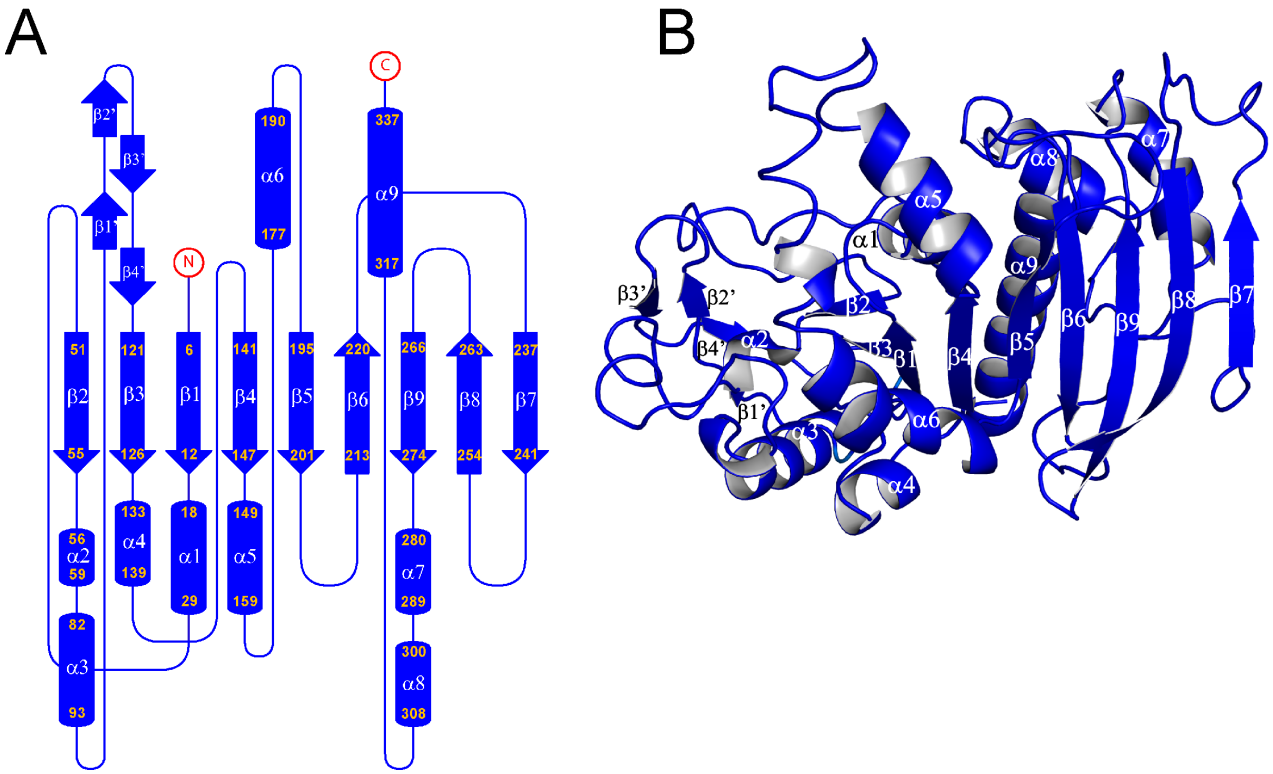

471

472

Figure 3

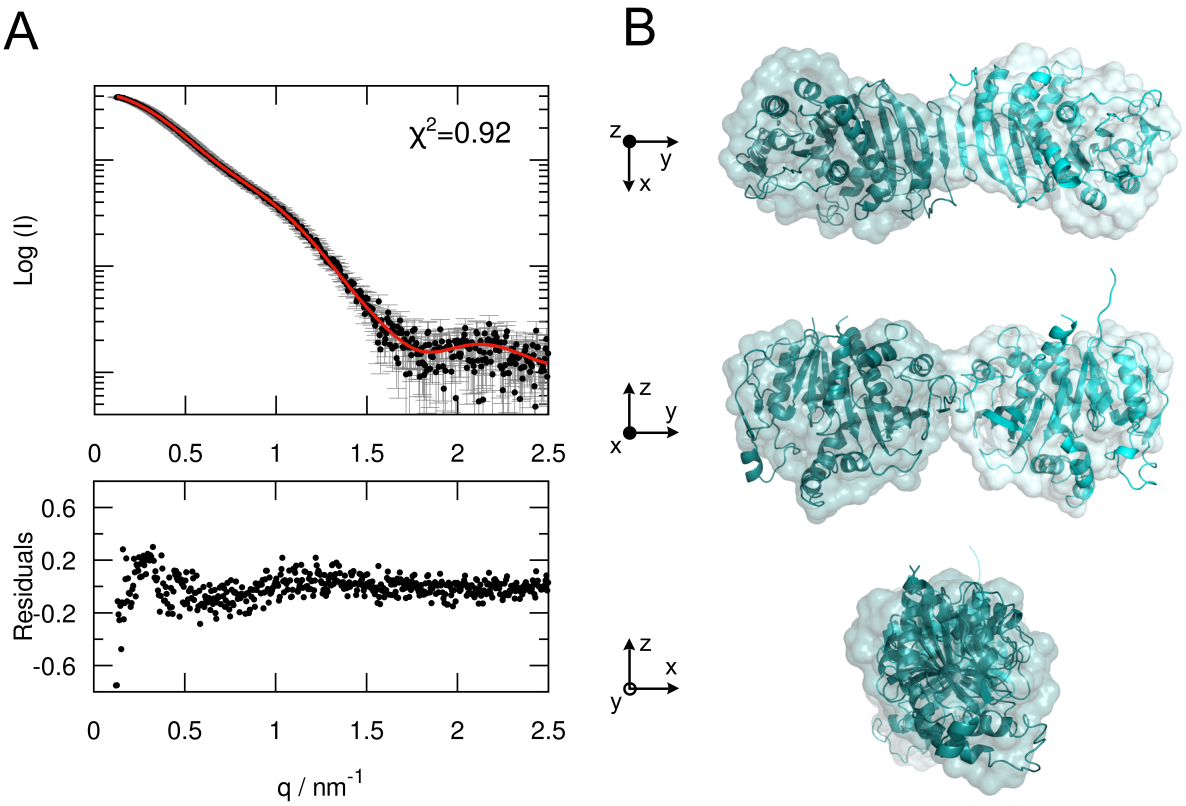

477 **Figure 4**

478

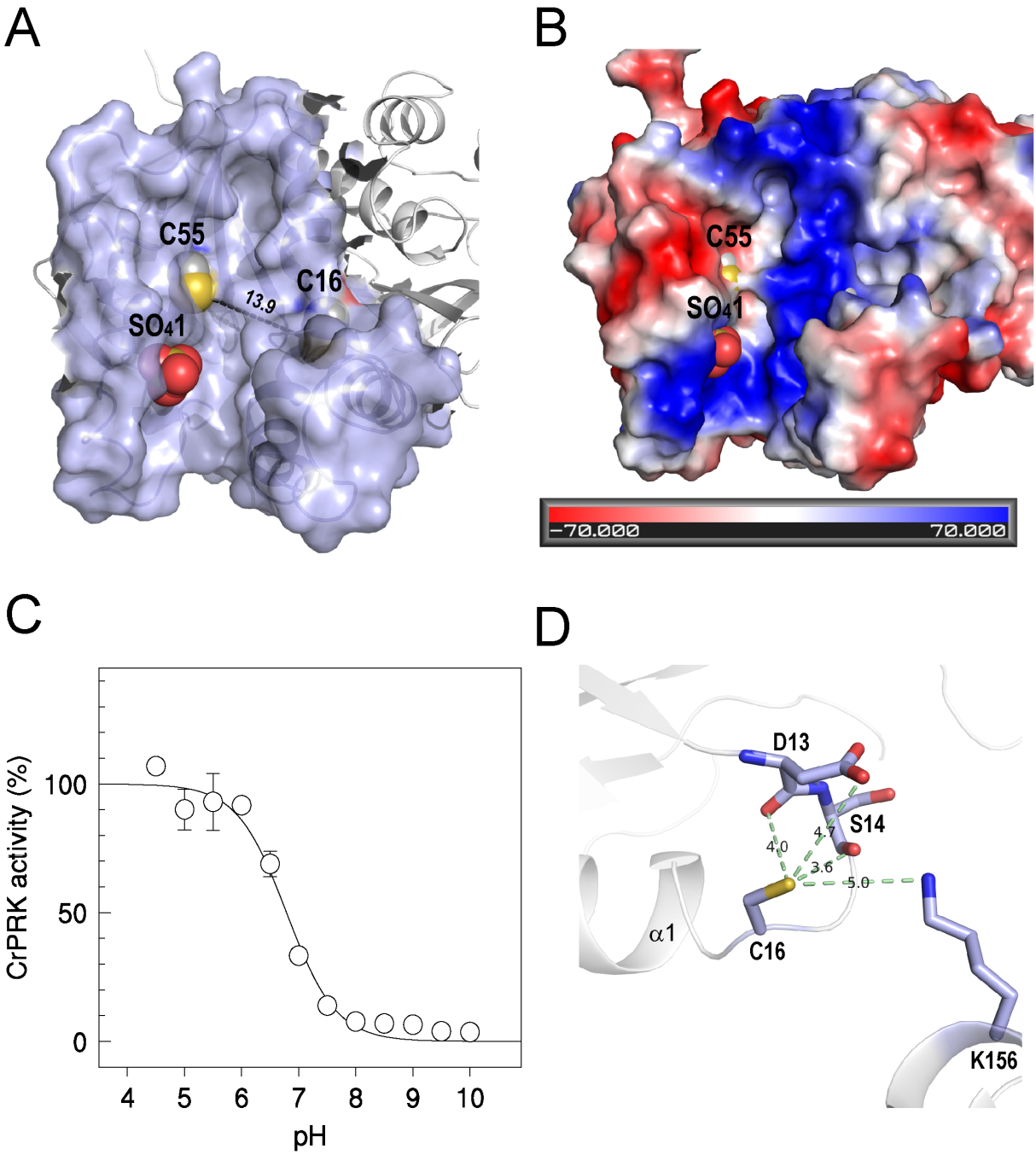

479

480

481 **Figure 5**

482

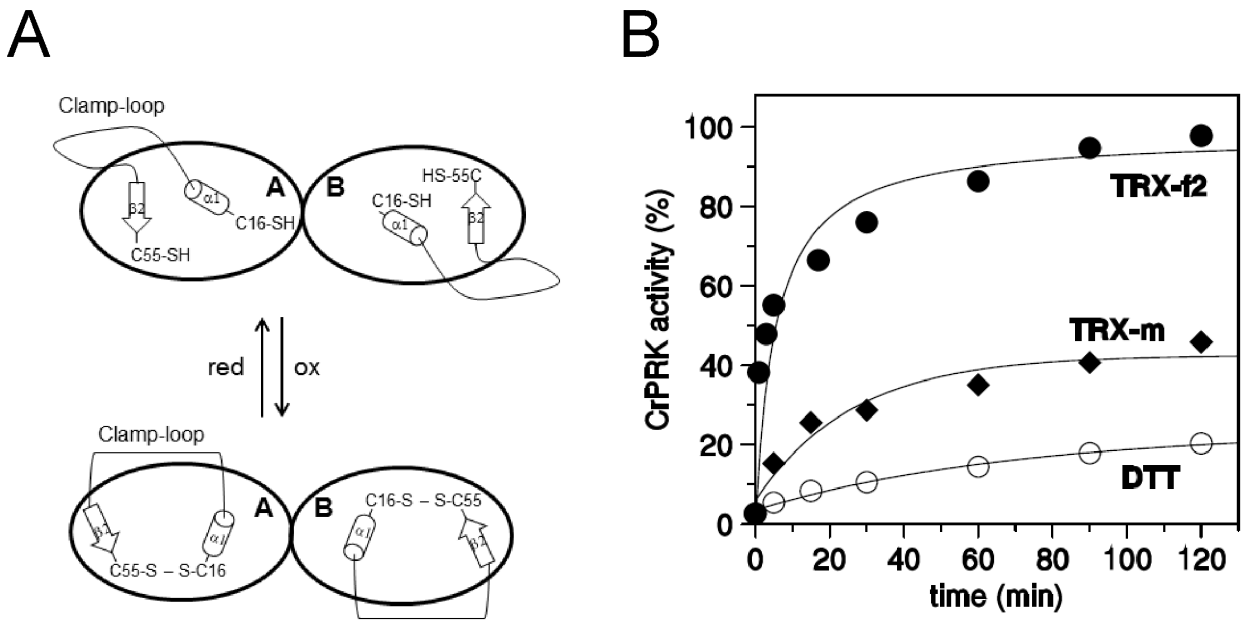

483

484